Highlights

- Neural trajectories in the hippocampus exhibited greater variability during a working memory (WM) task compared to those in the entorhinal cortex and amygdala regions.

- The distance of neural trajectories between encoding and retrieval states in the hippocampus was memory-load dependent during a WM task.

- Hippocampal neural trajectories fluctuated between the encoding and retrieval states in a task-dependent manner during both baseline and sharp-wave ripple (SWR) periods.

- Hippocampal neural trajectories shifted from encoding to retrieval states during SWR period.

Hippocampal neural fluctuations between memory encoding and retrieval states during a working memory task in humans: Encoding-to-retrieval shift during sharp-wave ripples

Yusuke Watanabe[a,*], Yuji Ikegaya[b,c,d], Takufumi Yanagisawa[a,e]

[a]*Institute for Advanced Cocreation studies, Osaka University, 2-2 Yamadaoka, Suita, 565-0871, Osaka, Japan*
[b]*Graduate School of Pharmaceutical Sciences, The University of Tokyo, 7-3-1 Hongo, Tokyo, 113-0033, Japan*
[c]*Institute for AI and Beyond, The University of Tokyo, 7-3-1 Hongo, Tokyo, 113-0033, Japan*
[d]*Center for Information and Neural Networks, National Institute of Information and Communications Technology, 1-4 Yamadaoka, Suita City, 565-0871, Osaka, Japan*
[e]*Department of Neurosurgery, Osaka University Graduate School of Medicine, 2-2 Yamadaoka, Osaka, 565-0871, Japan*

Abstract

Working memory (WM) is vital to a myriad of cognitive functions, yet its underlying neural mechanisms remain partially understood. The roles that the hippocampus and sharp-wave ripple complexes (SWRs) – which are brief, synchronizing neural events within the hippocampus – play in memory consolidation and retrieval, have increasingly garnered attention. Despite this, the interplay between these elements and WM tasks remains uncertain. Emerging research suggests that multiunit activity patterns within the hippocampus may operate in conjunction with SWRs, displaying unique dynamics during WM tasks. We examined an electroencephalogram dataset from the medial temporal lobe (MTL) in nine epilepsy patients undertaking an eight-second Sternberg task. Low-dimensional neural representations, also known as 'trajectories,' from MTL regions were extracted using Gaussian-process factor analysis during the execution of the WM task. Results show a significant variability in hippocampal neural trajectories, in contrast to those from the entorhinal cortex and the amygdala. Moreover, the trajectory dissimilarity between the encoding and retrieval phases appears to be contingent on memory load. Importantly, hippocampal trajectories oscillate during the retrieval phase, indicating task-dependent shifts between respective encoding and retrieval states, which occur during baseline and SWR events alike. These oscillations transition from encoding to retrieval states in synchrony with the occurrence of SWRs. This demonstrates the vital role played by the hippocampus in WM tasks and advances a new hypothesis: the functional state of the hippocampus transitions from encoding to retrieval during SWRs.

Keywords: working memory, WM, memory load, hippocampus, sharp-wave ripples, SWR, humans

---

1. Introduction

Working memory (WM) plays a crucial role in everyday life, yet its underlying neural mechanisms remain to be fully elucidated. Particularly, the function of the hippocampus, a vital brain region contributing to memory, commands ongoing investigation [1, 2, 3, 4, 5, 6, 7, 8, 9]. Gaining insight into the role of the hippocampus in working memory fosters a deeper understanding of cognitive processes and facilitates the development of cognitive training strategies and interventions.

Transient and synchronous oscillations, referred to as sharp wave ripples (SWR), are known to be associated with various cognitive functions, including mem-

*Corresponding author. Tel: +81-6-6879-3652

ory replay [10, 11, 12, 13], memory consolidation [14, 15, 16, 17], memory recall [18, 19, 20], and neural plasticity [21, 22]. Therefore, SWR might constitute a fundamental aspect of processing in the hippocampus and contribute to working memory performance. However, studies investigating the effects of SWRs on working memory remain scarce [23], and are predominantly limited to rodent models using navigation tasks, in which the exact timings of memory acquisition and recall are not distinguished.

Further, it has been discovered that hippocampal neurons exhibit low-dimensional representations during WM tasks. For instance, the firing patterns of place cells [24, 25, 26, 27, 28, 29] in the hippocampus are embedded within a dynamic, nonlinear three-dimensional hyperbolic geometry in rodents [30]. Moreover, grid cells in the entorhinal cortex (EC) — the primary gateway to the hippocampus [31, 32, 33] — displayed toroidal topology during exploration [34]. Nevertheless, these experiments are again constrained to spatial navigation tasks in rodents, limited in temporal resolution for WM tasks. Additionally, it has yet to be investigated whether these findings can be generalized to humans and tasks beyond navigation.

In light of these considerations, this study explores the hypothesis that hippocampal neurons exhibit distinct representations in low-dimensional spaces as a 'neural trajectory' during WM tasks, with a particular emphasis on SWR periods. To test this hypothesis, we utilized a dataset of patients performing an eight-second Sternberg task (with high temporal resolution: 1 s for fixation, 2 s for encoding, 3 s for maintenance, and 2 s for retrieval) while their intracranial electroencephalography signals (iEEG) in the medial temporal lobe (MTL) were being recorded [35]. We employed Gaussian-process factor analysis (GPFA) based on multiunit activities to explore low-dimensional neural trajectories, a known tool for analyzing neural population dynamics [36]. '''tex

2. Methods

2.1. Dataset

We utilized a publicly accessible dataset [35] wherein nine epilepsy patients performed a modified Sternberg task comprising the following four phases: fixation (1 s), encoding (2 s), maintenance (3 s), and retrieval (2 s) [35]. During the encoding phase, participants were presented with sets of four, six, or eight alphabetical letters, which we refer to as the set size. Subsequently, participants' task was to determine whether a probe letter presented during the retrieval phase had been previously displayed (the correct choice for the Match IN task) or not (the correct choice for the Mismatch OUT task). Intracranial EEG (iEEG) signals were captured using depth electrodes implanted within the medial temporal lobe (MTL) regions: the left and right hippocampal head (AHL and AHR), hippocampal body (PHL and PHR), entorhinal cortex (ECL and ECR), and amygdala (AL and AR). These signals were recorded at a sampling rate of 32 kHz and within the frequency range of 0.5–5,000 Hz (Figure 4A and Table 1). The iEEG signals were then resampled at a rate of 2 kHz. We uncovered correlations between the experimental variables such as set size and accuracy rate (Figure ??S1). The times of multiunit spikes were estimated using a spike sorting algorithm [37] from the Combinato package ((`https://github.com/jniediek/combinato`)(Figure 4C).

2.2. Calculation of neural trajectories using GPFA

To derive the neural trajectories (referred to as factors; Figure 4D) within the hippocampus, entorhinal cortex (EC), and amygdala, we used GPFA [36] on multiunit activity data for each session (Figure 4D). We implemented GPFA using the elephant package ((`https://elephant.readthedocs.io/en/latest/reference/gpfa.html`). We configured the bin size as 50 ms, with no overlaps. Each factor was z-normalized across all sessions. We calculated the Euclidean distance from the origin (O) using these trajectories (Figure 4E).

Within each trajectory for a region such as AHL, we calculated the *geometric medians* (i.e., g_F for fixation, g_E for encoding, g_M for maintenance, and g_R for retrieval phase) by establishing the median coordinates of the trajectory during the four phases (Figure 4D). We defined the optimal dimensionality for GPFA as three, as determined via the elbow method using log-likelihood values in a three-fold cross-validation approach (Figure 2B).

2.3. Defining SWR candidates from hippocampal regions

To pinpoint potential SWR events in the hippocampus, we used a detection method consistent with the consensus in the field [38]. We re-referenced local field potential (LFP) signals from a region of interest (ROI), such as AHL, by subtracting the average signal outside the ROI (e.g., AHR, PHL, PHR, ECL, ECR, AL, AR) (see Figure 4A). Using these re-referenced LFP signals, we applied a ripple-band filter (80–140 Hz) to isolate SWR-positive (SWR$^+$) candidates (see Figure 4B). We performed SWR detection using a publicly available tool ((`https://github.com/Eden-Kramer-Lab/ripple_detection`) [39], with some modifications such as a revised bandpass range of 80–140 Hz for human applications [19, 20] as opposed to the original 150–250 Hz range used primarily for rodents.

For SWR$^+$ candidates, we defined SWR-negative (SWR$^-$) candidates as control events by shuffling the timestamps of SWR$^+$ candidates across all trials and subjects. We visually inspected the defined SWR$^+$/SWR$^-$ candidates (see Figure 4).

2.4. Defining SWRs from putative hippocampal CA1 regions

We narrowed down SWR candidates within putative CA1 regions to define SWRs. We first identified putative CA1 regions as follows. We embedded SWR$^+$/SWR$^-$ candidates within the hippocampus into a two-dimensional space based on their superimposed spike counts per unit using UMAP (uniform manifold approximation and projection) [40] in a supervised manner (Figure 4A). The silhouette score [41], a validation metric for clustering, was calculated from clustered samples (Table 2). We defined hippocampal regions with an average silhouette score across sessions greater than the 75th percentile as putative CA1 regions, resulting in the identification of five electrode locations from five patients (Table 3).

We defined SWR$^+$/SWR$^-$ candidates within putative CA1 regions as SWRs, meaning they were no longer candidates. The duration and ripple band peak amplitude of SWRs followed log-normal distributions (Figure 4C & E). We visually inspected SWR$^+$/SWR$^-$ as shown in Figure 4. We divided each SWR period into pre-SWR (at −800 to −300 ms from SWR center), mid-SWR (at −250 to +250 ms), and post-SWR (at +300 to +800 ms) based on the time from the SWR's center.

2.5. Statistical Evaluation

We conducted the Brunner–Munzel and Kruskal-Wallis tests using the scipy package in Python [42]. We performed a correlation analysis by determining the rank of the observed correlation coefficient within the set-size-shuffled surrogate dataset, using a custom Python script. Additionally, we executed a bootstrap test using a homemade Python script.
"

3. Results

3.1. iEEG recording and neural trajectory in MTL regions during a Sternberg task

We utilized a publicly accessible dataset [35] for this analysis, which consists of LFP signals (Figure 1A) from MTL regions (Table 11) obtained during a modified Sternberg task. SWR$^+$ candidates were detected within all hippocampal regions from LFP signals, filtered by the ripple band (80–140 Hz) (Figure 1B), whereas SWR$^-$ candidates were defined at identical timestamps as SWR$^+$ candidates but shuffled across separate trials (Figure 1). The multiunit spikes (Figure 1C) were also included in the dataset, identified by implementation of a spike sorting algorithm [37]. Relying on the 50-ms binned multiunit activity devoid of overlaps, we applied GPFA [36] to elucidate the neural trajectory (or factors) of MTL regions by session and region (Figure 1D). Each factor was z-normalized by session and region (an instance being session #2 in AHL of subject #1). The Euclidean distance from the origin (O) was subsequently calculated (Figure 1E).

3.2. Hippocampal neural trajectory correlation with a Sternberg task

Figure 2A delineates the median neural trajectories of 50 trials as point clouds within the three primary factor space. The optimal embedding dimension for the GPFA model, determined by employing the elbow method, was found to be three (Figure 2B). The trajectory distance from the origin (O) ($\|g_F\|$, $\|g_E\|$, $\|g_M\|$, and $\|g_R\|$) was larger in the hippocampus than in the EC and

amygdala (Figure 2C & D).[1]

Similarly, the distances among geometric medians of the four phases: $\|g_Fg_E\|$, $\|g_Fg_M\|$, $\|g_Fg_R\|$, $\|g_Eg_M\|$, $\|g_Eg_R\|$, and $\|g_Mg_R\|$ were calculated, displaying that the hippocampus demonstrated larger distances among the phases compared to both the EC and amygdala. [2]

3.3. Memory load-dependent neural trajectory distance between the encoding and retrieval states in the hippocampus

Considering the memory load of the Stenberg task, the correct trial rate and set size (= the number of alphabet letters to encode) were negatively correlated (Figure 3A). [3] Likewise, response time and set size displayed a positive correlation (Figure 3B).[4]

Further, the set size and trajectory distance between the encoding and retrieval phases ($\log_{10}\|g_Eg_R\|$) exhibited a positive correlation (Figure 3C).[5], while distances between other phase combinations did not note any significant correlations (Figures 3D & S2).

3.4. Detection of hippocampal SWR from putative CA1 regions

With the intent of improving the accuracy of recording sites and SWR detection, we attempted to estimate electrodes in CA1 regions of the hippocampus by observing distinct multiunit spike patterns during SWR

occurrences. For each session and hippocampal region, SWR^+/SWR^- candidates were embedded into a two-dimensional space using UMAP (Figure 4A).[6] The silhouette score was calculated as a measure of clustering quality (Figure 4B & Table 2). Recording sites with an average silhouette score across sessions exceeding 0.6 were recognized as putative CA1 regions [40, 41] [7] (Tables 2 & 3). Hence, we identified five putative CA1 regions, four of which were not previously labeled as seizure onset zones (Table 1).

Subsequently, we labeled SWR^+/SWR^- candidates within these putative CA1 regions as SWR^+ and SWR^-, respectively[8] (Table 3). Both SWR^+ and SWR^- exhibited the same duration[9] (Figure 4C) as per their definitions, following a log-distribution profile. A notable uptick in SWR^+ incidence appeared during the initial 400 ms of the retrieval phase [10] (Figure 4D). Besides, the peak ripple band amplitude of SWR^+ exceeded that of SWR^-, following a log-normal distribution (Figure 4E).[11].

3.5. Transient change in neural trajectory in the hippocampus during SWR

We analyzed the *distances* of the trajectory from origin (O) during SWR events in both encoding and retrieval phases (Figure 5A). Given the increase in distance during SWR, as shown in Figure 5A, we classified each SWR into three stages: pre-, mid-, and post-SWR. Thereafter, the distances from O during these SWR periods are represented as $\|pre\text{-}eSWR^+\|$, $\|mid\text{-}eSWR^+\|$, and so forth.

$\|mid\text{-}eSWR^+\|$ [12] was larger than $\|pre\text{-}eSWR^+\|$ [13],

---

[1] Hippocampus: Distance = 1.11 [1.01], median [IQR], n = 195,681 timepoints; EC: Distance = 0.94 [1.10], median [IQR], n = 133,761 timepoints; Amygdala: Distance = 0.78 [0.88], median [IQR], n = 165,281 timepoints.

[2] Hippocampus: Distance = 0.60 [0.70], median [IQR], n = 8,772 combinations; EC: Distance = 0.28 [0.52], median [IQR], n = 5,017 combinations (p < 0.01; Brunner–Munzel test); Amygdala: Distance = 0.24 [0.42], median [IQR], n = 7,466 combinations (p < 0.01; Brunner–Munzel test).

[3] Correct rate: set size four (0.99 ±0.11, mean ±SD; n = 333 trials) vs. set size six (0.93 ±0.26; n = 278 trials) and set size eight (0.87 ±0.34; n = 275 trials; p < 0.05; Brunner–Munzel test with Bonferroni correction). Overall, p < 0.001 for Kruskal–Wallis test; correlation coefficient = - 0.20, p < 0.001.

[4] Response time: set size four (1.26 ±0.45 s; n = 333 trials) vs. set size six (1.53 ±0.91 s; n = 278 trials) and set size eight (1.66 ±0.80 s; n = 275 trials). All comparisons p < 0.001, Brunner–Munzel test with Bonferroni correction; p < 0.001 for Kruskal–Wallis test; correlation coefficient = 0.22, p < 0.001

[5] Correlation between set size and $\log_{10}(\|g_Eg_R\|)$: correlation coefficient = 0.05, p < 0.001. Specific values: $\|g_Eg_R\|$ = 0.54 [0.70] for set size four trials, n = 447; $\|g_Eg_R\|$ = 0.58 [0.66] for set size six trials, n = 381; $\|g_Eg_R\|$ = 0.61 [0.63] for set size eight trials, n = 395.

[6] For illustrative purposes, consider the AHL in session #1 of subject #1.

[7] The regions identified were: AHL of subject #1, AHR of subject #3, PHL of subject #4, AHL of subject #6, and AHR of subject #9.

[8] Defining them resulted in equal counts for both categories: SWR^+ (n = 1,170) and SWR^- (n = 1,170).

[9] Defining them resulted in identical duration for both categories: SWR^+ (93.0 [65.4] ms) and SWR^- (93.0 [65.4] ms).

[10] SWR^+ increased against the bootstrap sample; 95th percentile = 0.42 [Hz]; p < 0.05.

[11] SWR^+ (3.05 [0.85] SD of baseline, median [IQR]; n = 1,170) vs. SWR^- (2.37 [0.33] SD of baseline, median [IQR]; n = 1,170; p < 0.001; Brunner–Munzel test).

[12] 1.25 [1.30], median [IQR], n = 1,281, in Match IN task; 1.12 [1.35], median [IQR], n = 1,163, in Mismatch OUT task

[13] 1.08 [1.07], median [IQR], n = 1,149, in Match IN task; 0.90 [1.12], median [IQR], n = 1,088, in Mismatch OUT task

and $\|$mid-rSWR$^+\|$ [14] was larger than $\|$pre-rSWR$^+\|$ in both Match IN and Mismatch OUT tasks. [15]

3.6. Visualization of hippocampal neural trajectory during SWR in two-dimensional spaces

Given our observations of neural trajectory 'jump' during SWR (Figure 5), we visualized the three-dimensional trajectories of pre-, mid-, and post-SWR events during the encoding and retrieval phases (Figure 6), the distance between which was dependent on memory-load (Figure 3).

We accomplished the visualization in two-dimensional spaces by linearly aligning peri-SWR trajectories, positioning g_E at the origin (0, 0) and g_R at the coordinate ($\|g_E g_R\|$, 0). These aligned trajectories were then rotated around the $g_E g_R$ axis (= x-axis), ensuring conservation of distances from the origin O and angles between $g_E g_R$ in the original three-dimensional spaces in the two-dimensional spaces.

The scatter plot in these two-dimensional spaces portrays the distinctive distributions of peri-SWR trajectories based on phases and task types. For instance, one can distinguish that $\|$mid-eSWR$^+\|$ is larger than $\|$pre-eSWR$^+\|$ (Figure 6B), consistent with our earlier findings (Figure 5).

3.7. Fluctuating hippocampal neural trajectories between encoding and retrieval states

Following this, we inspected the trajectory *directions* based on $\overrightarrow{g_E g_R}$. Directions of SWRs were identified by the neural trajectory at −250 ms and +250 ms from their center (i.e., $\overrightarrow{eSWR^+}$).

We computed the density of $\overrightarrow{eSWR} \cdot \overrightarrow{g_E g_R}$, $\overrightarrow{rSWR} \cdot \overrightarrow{g_E g_R}$, and $\overrightarrow{eSWR} \cdot \overrightarrow{rSWR}$ (Figure 7A–D). $\overrightarrow{rSWR^-} \cdot \overrightarrow{g_E g_R}$ exhibited biphasic distributions.

By comparing the distribution of $\overrightarrow{rSWR^+} \cdot \overrightarrow{g_E g_R}$ (Figures 7A & B) with those of $\overrightarrow{rSWR^-} \cdot \overrightarrow{g_E g_R}$ (Figures 7C & D), we calculated the contributions of SWR (Figures 7E & F), which unveiled a shift in the direction of $\overrightarrow{g_E g_R}$ (Figures 7E & F; see *red rectangles*).

Additionally, only in the Mismatch OUT task was

$\overrightarrow{eSWR^+} \cdot \overrightarrow{rSWR^+}$ less than that of $\overrightarrow{eSWR^-} \cdot \overrightarrow{rSWR^-}$ (baseline periods) (Figure 7F; see *pink circles*); stated differently, eSWRs and rSWRs directed in the opposing direction exclusively in the Mismatch OUT task but not in the Match IN task (Figure 7E; see *pink circles*).

4. Discussion

This study posited that hippocampal neurons demonstrate unique representations, or trajectories, in low-dimensional spaces during a working memory (WM) task in humans, specifically during sharp-wave ripple (SWR) periods. Initially, we projected the multiunit spikes from medial temporal lobe regions during a Sternberg task onto three-dimensional spaces using Gaussian-process factor analysis (GPFA) (Figure 4D–E and Figure 2A) [36]. The trajectory distance among WM phases ($\|g_F g_E\|$, $\|g_F g_M\|$, $\|g_F g_R\|$, $\|g_E g_M\|$, $\|g_E g_R\|$, and $\|g_M g_R\|$) was larger in the hippocampus than in the entorhinal cortex (EC) and amygdala (Figure 2E), indicating more dynamic neural activity in the hippocampus during the WM task. Moreover, the trajectory distance between the encoding and retrieval phases in the hippocampus ($\|g_F g_E\|$) positively correlated with memory load (Figure 3C–D), thereby marking it as a reflection of WM processing. The neural trajectory in the hippocampus also exhibited a transient increase during SWRs (Figure 5). Lastly, the hippocampal neural trajectory fluctuated between encoding and retrieval states, transitioning from encoding to retrieval during SWR events (Figure 7). Overall, these findings highlight the role of hippocampal neural activity in a WM task in humans [31, 32, 33].

We discovered that the neural trajectory's distance among the four phases was longer in the hippocampus compared to the EC and amygdala, even when adjusting for the distance from origin O ($\|g_F\|$, $\|g_E\|$, $\|g_M\|$, and $\|g_R\|$) in those regions (Figure 2C–E). These findings corroborate the role of the hippocampus in the WM task, which aligns with previous reports of hippocampal persistent firing in the maintenance phase [3] [4] [5] [6]. However, by applying GPFA to multiunit activity during a one-second level resolution of WM task, we found that the low dimensional space neural trajectory exhibits a memory-load dependency between the encoding and retrieval phases, represented as $\|g_E g_R\|$ (Figure 3). These

---

[14] 1.32 [1.24], median [IQR], $n = 935$, in Match IN task; 1.15 [1.26], median [IQR], $n = 891$, in Mismatch OUT task

[15] 1.19 [0.96], median [IQR], $n = 673$, in Match IN task; 0.94 [0.88], median [IQR], $n = 664$, in Mismatch OUT task

results reaffirm the association between the hippocampus and WM processing [?].

The reliability of our analysis, restricted to presumed CA1 regions (Figure 4), is supported by several contributing factors. This focused approach is grounded in consistent observations that SWRs are synchronous with spike bursts of interneurons and pyramidal neurons [43] [44] [29] [45], potentially within a $50\,\mu m$ radius of the recording site [46]. In this study, we observed an increase in SWR occurrences at 0–400 ms of the retrieval phase (Figure 4D), aligning with prior studies demonstrating increased SWR occurrences before spontaneous verbal recall [19] [20]. This finding not only corroborates but broadens the observation to a triggered retrieval condition. Additionally, the log-normal distributions of SWR duration and ripple band peak amplitude observed in this study (Figure 4C E) correlate with the consensus in this field [38]. Hence, our approach of confining recording sites to probable CA1 regions likely improved the precision of SWR detection. It should be noted that an increase in trajectory distance from origin O during SWR (Figure 5) may have been skewed to a greater extent due to the channel selection; however, this does not dramatically impact our primary findings.

Interestingly, trajectory directions in the retrieval phase oscillated between encoding and retrieval states both in baseline and SWR periods (Figure 7C & D). Furthermore, the balance of these fluctuations transitioned from encoding to retrieval states during SWR (Figure 7E & F). These findings concur with previous studies suggesting SWR's role in memory recall [19] [20]. Our results add another layer of understanding, specifying that SWRs occur when hippocampal representation transitions from encoding to retrieval states. Therefore, our findings offer new insights into hippocampal representations: (i) neural fluctuations between encoding and retrieval states during a WM task and (ii) SWR as a mechanism facilitating the transition from encoding to retrieval states [47].

Additionally, our research reveals WM-task-specific directions between encoding and retrieval SWRs (Figure 7E–F). Particularly, encoding SWR and retrieval SWR pointed in opposing directions not in a Match IN but in a Mismatch OUT task. These results might align with the memory engram theory [48]. Indeed, the Match In task showed subjects a once-seen letter, while the Mismatch OUT task presented a novel letter not introduced in the encoding phase. These outcomes suggest that SWR relates to the working cognitive processes in humans.

In conclusion, our study has demonstrated that hippocampal activity fluctuates between encoding and retrieval states during a WM task and undergoes a significant shift from encoding to retrieval during SWR periods.

References

[1] W. B. Scoville, B. Milner, LOSS OF RECENT MEMORY AFTER BILATERAL HIPPOCAMPAL LESIONS, Journal of Neurology, Neurosurgery, and Psychiatry 20 (1) (1957) 11–21. URL https://www.ncbi.nlm.nih.gov/pmc/articles/PMC497229/

[2] L. R. Squire, The Legacy of Patient H.M. for Neuroscience, Neuron 61 (1) (2009) 6–9. doi:10.1016/j.neuron.2008.12.023. URL https://www.ncbi.nlm.nih.gov/pmc/articles/PMC2649674/

[3] E. Boran, T. Fedele, P. Klaver, P. Hilfiker, L. Stieglitz, T. Grunwald, J. Sarnthein, Persistent hippocampal neural firing and hippocampal-cortical coupling predict verbal working memory load, Science Advances 5 (3) (2019) eaav3687. doi:10.1126/sciadv.aav3687. URL https://www.science.org/doi/10.1126/sciadv.aav3687

[4] J. Kamiński, S. Sullivan, J. M. Chung, I. B. Ross, A. N. Mamelak, U. Rutishauser, Persistently active neurons in human medial frontal and medial temporal lobe support working memory, Nature Neuroscience 20 (4) (2017) 590–601, number: 4 Publisher: Nature Publishing Group. doi:10.1038/nn.4509. URL https://www.nature.com/articles/nn.4509

[5] S. Kornblith, R. Q. Quiroga, C. Koch, I. Fried, F. Mormann, Persistent Single-Neuron Activity during Working Memory in the Human Medial Temporal Lobe, Current Biology 27 (7) (2017) 1026–1032, publisher: Elsevier. doi:10.1016/j.cub.2017.02.013. URL https://www.cell.com/current-biology/abstract/S0960-9822(17)30149-5

[6] M. C. M. Faraut, A. A. Carlson, S. Sullivan, O. Tudusciuc, I. Ross, C. M. Reed, J. M. Chung, A. N. Mamelak, U. Rutishauser, Dataset of human medial temporal lobe single neuron activity during declarative memory encoding and recognition, Scientific Data 5 (1) (2018) 180010, number: 1 Publisher: Nature Publishing Group. doi:10.1038/sdata.2018.10. URL https://www.nature.com/articles/sdata201810

[7] A. A. Borders, C. Ranganath, A. P. Yonelinas, The hippocampus supports high-precision binding in visual working memory, Hippocampus 32 (3) (2022) 217–230. doi:10.1002/hipo.23401.

[8] J. Li, D. Cao, S. Yu, X. Xiao, L. Imbach, L. Stieglitz, J. Sarnthein, T. Jiang, Functional specialization and interaction in the amygdala-hippocampus circuit during working memory processing, Nature Communications 14 (1) (2023)

2921, number: 1 Publisher: Nature Publishing Group. doi:10.1038/s41467-023-38571-w.
URL https://www.nature.com/articles/s41467-023-38571-w

[9] V. Dimakopoulos, P. Mégevand, L. H. Stieglitz, L. Imbach, J. Sarnthein, Information flows from hippocampus to auditory cortex during replay of verbal working memory items, eLife 11 (2022) e78677, publisher: eLife Sciences Publications, Ltd. doi:10.7554/eLife.78677.
URL https://doi.org/10.7554/eLife.78677

[10] M. A. Wilson, B. L. McNaughton, Reactivation of hippocampal ensemble memories during sleep, Science (New York, N.Y.) 265 (5172) (1994) 676–679. doi:10.1126/science.8036517.

[11] Z. Nádasdy, H. Hirase, A. Czurkó, J. Csicsvari, G. Buzsáki, Replay and Time Compression of Recurring Spike Sequences in the Hippocampus, Journal of Neuroscience 19 (21) (1999) 9497–9507, publisher: Society for Neuroscience Section: ARTICLE. doi:10.1523/JNEUROSCI.19-21-09497.1999.
URL https://www.jneurosci.org/content/19/21/9497

[12] A. K. Lee, M. A. Wilson, Memory of sequential experience in the hippocampus during slow wave sleep, Neuron 36 (6) (2002) 1183–1194. doi:10.1016/s0896-6273(02)01096-6.

[13] T. J. Davidson, F. Kloosterman, M. A. Wilson, Hippocampal replay of extended experience, Neuron 63 (4) (2009) 497–507. doi:10.1016/j.neuron.2009.07.027.

[14] G. Girardeau, K. Benchenane, S. I. Wiener, G. Buzsáki, M. B. Zugaro, Selective suppression of hippocampal ripples impairs spatial memory, Nature Neuroscience 12 (10) (2009) 1222–1223. doi:10.1038/nn.2384.
URL http://www.nature.com/articles/nn.2384

[15] V. Ego-Stengel, M. A. Wilson, Disruption of ripple-associated hippocampal activity during rest impairs spatial learning in the rat, Hippocampus 20 (1) (2010) 1–10. doi:10.1002/hipo.20707.

[16] A. Fernández-Ruiz, A. Oliva, E. Fermino de Oliveira, F. Rocha-Almeida, D. Tingley, G. Buzsáki, Long-duration hippocampal sharp wave ripples improve memory, Science (New York, N.Y.) 364 (6445) (2019) 1082–1086. doi:10.1126/science.aax0758.
URL https://www.ncbi.nlm.nih.gov/pmc/articles/PMC6693581/

[17] J. Kim, A. Joshi, L. Frank, K. Ganguly, Cortical–hippocampal coupling during manifold exploration in motor cortex, Nature (2022) 1–8Publisher: Nature Publishing Group. doi:10.1038/s41586-022-05533-z.
URL https://www.nature.com/articles/s41586-022-05533-z

[18] C.-T. Wu, D. Haggerty, C. Kemere, D. Ji, Hippocampal awake replay in fear memory retrieval, Nature Neuroscience 20 (4) (2017) 571–580. doi:10.1038/nn.4507.

[19] Y. Norman, E. M. Yeagle, S. Khuvis, M. Harel, A. D. Mehta, R. Malach, Hippocampal sharp-wave ripples linked to visual episodic recollection in humans, Science 365 (6454) (2019) eaax1030. doi:10.1126/science.aax1030.
URL https://www.sciencemag.org/lookup/doi/10.1126/science.aax1030

[20] Y. Norman, O. Raccah, S. Liu, J. Parvizi, R. Malach, Hip-

pocampal ripples and their coordinated dialogue with the default mode network during recent and remote recollection, Neuron 109 (17) (2021) 2767–2780.e5, publisher: Elsevier. doi:10.1016/j.neuron.2021.06.020.
URL https://www.cell.com/neuron/abstract/S0896-6273(21)00461-X

[21] C. J. Behrens, L. P. van den Boom, L. de Hoz, A. Friedman, U. Heinemann, Induction of sharp wave–ripple complexes in vitro and reorganization of hippocampal networks, Nature Neuroscience 8 (11) (2005) 1560–1567, number: 11 Publisher: Nature Publishing Group. doi:10.1038/nn1571.
URL https://www.nature.com/articles/nn1571

[22] H. Norimoto, K. Makino, M. Gao, Y. Shikano, K. Okamoto, T. Ishikawa, T. Sasaki, H. Hioki, S. Fujisawa, Y. Ikegaya, Hippocampal ripples down-regulate synapses, Science (New York, N.Y.) 359 (6383) (2018) 1524–1527. doi:10.1126/science.aao0702.

[23] S. P. Jadhav, C. Kemere, P. W. German, L. M. Frank, Awake Hippocampal Sharp-Wave Ripples Support Spatial Memory, Science 336 (6087) (2012) 1454–1458, publisher: American Association for the Advancement of Science. doi:10.1126/science.1217230.
URL https://www.science.org/doi/abs/10.1126/science.1217230

[24] J. O'Keefe, J. Dostrovsky, The hippocampus as a spatial map: Preliminary evidence from unit activity in the freely-moving rat, Brain Research 34 (1971) 171–175, place: Netherlands Publisher: Elsevier Science. doi:10.1016/0006-8993(71)90358-1.

[25] J. O'Keefe, Place units in the hippocampus of the freely moving rat, Experimental Neurology 51 (1) (1976) 78–109. doi:10.1016/0014-4886(76)90055-8.
URL https://www.sciencedirect.com/science/article/pii/0014488676900558

[26] A. D. Ekstrom, M. J. Kahana, J. B. Caplan, T. A. Fields, E. A. Isham, E. L. Newman, I. Fried, Cellular networks underlying human spatial navigation, Nature 425 (6954) (2003) 184–188, number: 6954 Publisher: Nature Publishing Group. doi:10.1038/nature01964.
URL https://www.nature.com/articles/nature01964

[27] K. B. Kjelstrup, T. Solstad, V. H. Brun, T. Hafting, S. Leutgeb, M. P. Witter, E. I. Moser, M.-B. Moser, Finite Scale of Spatial Representation in the Hippocampus, Science 321 (5885) (2008) 140–143, publisher: American Association for the Advancement of Science. doi:10.1126/science.1157086.
URL https://www.science.org/doi/abs/10.1126/science.1157086

[28] C. D. Harvey, F. Collman, D. A. Dombeck, D. W. Tank, Intracellular dynamics of hippocampal place cells during virtual navigation, Nature 461 (7266) (2009) 941–946, number: 7266 Publisher: Nature Publishing Group. doi:10.1038/nature08499.
URL https://www.nature.com/articles/nature08499

[29] S. Royer, B. V. Zemelman, A. Losonczy, J. Kim, F. Chance, J. C. Magee, G. Buzsáki, Control of timing, rate and bursts of hippocampal place cells by dendritic and somatic inhibition, Nature Neuroscience 15 (5) (2012) 769–775, number: 5 Publisher: Nature Publishing Group. doi:10.1038/nn.3077.
URL https://www.nature.com/articles/nn.3077

[30] H. Zhang, P. D. Rich, A. K. Lee, T. O. Sharpee, Hippocampal spatial representations exhibit a hyperbolic geometry that expands with experience, Nature Neuroscience (Dec. 2022). doi:10.1038/s41593-022-01212-4.
URL https://www.nature.com/articles/s41593-022-01212-4

[31] P. A. Naber, F. H. Lopes da Silva, M. P. Witter, Reciprocal connections between the entorhinal cortex and hippocampal fields CA1 and the subiculum are in register with the projections from CA1 to the subiculum, Hippocampus 11 (2) (2001) 99–104, _eprint: https://onlinelibrary.wiley.com/doi/pdf/10.1002/hipo.1028. doi:10.1002/hipo.1028.
URL https://onlinelibrary.wiley.com/doi/abs/10.1002/hipo.1028

[32] N. M. van Strien, N. L. M. Cappaert, M. P. Witter, The anatomy of memory: an interactive overview of the parahippocampal–hippocampal network, Nature Reviews Neuroscience 10 (4) (2009) 272–282, number: 4 Publisher: Nature Publishing Group. doi:10.1038/nrn2614.
URL https://www.nature.com/articles/nrn2614

[33] B. A. Strange, M. P. Witter, E. S. Lein, E. I. Moser, Functional organization of the hippocampal longitudinal axis, Nature Reviews Neuroscience 15 (10) (2014) 655–669, number: 10 Publisher: Nature Publishing Group. doi:10.1038/nrn3785.
URL https://www.nature.com/articles/nrn3785

[34] R. J. Gardner, E. Hermansen, M. Pachitariu, Y. Burak, N. A. Baas, B. A. Dunn, M.-B. Moser, E. I. Moser, Toroidal topology of population activity in grid cells, Nature 602 (7895) (2022) 123–128, number: 7895 Publisher: Nature Publishing Group. doi:10.1038/s41586-021-04268-7.
URL https://www.nature.com/articles/s41586-021-04268-7

[35] E. Boran, T. Fedele, A. Steiner, P. Hilfiker, L. Stieglitz, T. Grunwald, J. Sarnthein, Dataset of human medial temporal lobe neurons, scalp and intracranial EEG during a verbal working memory task, Scientific Data 7 (1) (2020) 30, number: 1 Publisher: Nature Publishing Group. doi:10.1038/s41597-020-0364-3.
URL https://www.nature.com/articles/s41597-020-0364-3

[36] B. M. Yu, J. P. Cunningham, G. Santhanam, S. I. Ryu, K. V. Shenoy, M. Sahani, Gaussian-Process Factor Analysis for Low-Dimensional Single-Trial Analysis of Neural Population Activity, Journal of Neurophysiology 102 (1) (2009) 614–635. doi:10.1152/jn.90941.2008.
URL https://www.ncbi.nlm.nih.gov/pmc/articles/PMC2712272/

[37] J. Niediek, J. Boström, C. E. Elger, F. Mormann, Reliable Analysis of Single-Unit Recordings from the Human Brain under Noisy Conditions: Tracking Neurons over Hours, PLOS ONE 11 (12) (2016) e0166598, publisher: Public Library of Science. doi:10.1371/journal.pone.0166598.
URL https://journals.plos.org/plosone/article?id=10.1371/journal.pone.0166598

[38] A. A. Liu, S. Henin, S. Abbaspoor, A. Bragin, E. A. Buffalo, J. S. Farrell, D. J. Foster, L. M. Frank, T. Gedankien, J. Gotman, J. A. Guidera, K. L. Hoffman, J. Jacobs, M. J. Kahana, L. Li, Z. Liao, J. J. Lin, A. Losonczy, R. Malach, M. A. van der Meer, K. McClain, B. L. McNaughton, Y. Norman, A. Navas-Olive, L. M. de la Prida, J. W. Rueckemann, J. J. Sakon, I. Skelin, I. Soltesz, B. P. Staresina, S. A. Weiss, M. A. Wilson, K. A. Zaghloul, M. Zugaro, G. Buzsáki, A consensus statement on detection of hippocampal sharp wave ripples and differentiation from other fast oscillations, Nature Communications 13 (1) (2022) 6000, number: 1 Publisher: Nature Publishing Group. doi:10.1038/s41467-022-33536-x.
URL https://www.nature.com/articles/s41467-022-33536-x

[39] K. Kay, M. Sosa, J. E. Chung, M. P. Karlsson, M. C. Larkin, L. M. Frank, A hippocampal network for spatial coding during immobility and sleep, Nature 531 (7593) (2016) 185–190. doi:10.1038/nature17144.

[40] L. McInnes, J. Healy, N. Saul, L. Großberger, UMAP: Uniform Manifold Approximation and Projection, Journal of Open Source Software 3 (29) (2018) 861. doi:10.21105/joss.00861.
URL https://joss.theoj.org/papers/10.21105/joss.00861

[41] P. J. Rousseeuw, Silhouettes: A graphical aid to the interpretation and validation of cluster analysis, Journal of Computational and Applied Mathematics 20 (1987) 53–65. doi:10.1016/0377-0427(87)90125-7.
URL https://www.sciencedirect.com/science/article/pii/0377042787901257

[42] P. Virtanen, R. Gommers, T. E. Oliphant, M. Haberland, T. Reddy, D. Cournapeau, E. Burovski, P. Peterson, W. Weckesser, J. Bright, S. J. van der Walt, M. Brett, J. Wilson, K. J. Millman, N. Mayorov, A. R. J. Nelson, E. Jones, R. Kern, E. Larson, C. J. Carey, Polat, Y. Feng, E. W. Moore, J. VanderPlas, D. Laxalde, J. Perktold, R. Cimrman, I. Henriksen, E. A. Quintero, C. R. Harris, A. M. Archibald, A. H. Ribeiro, F. Pedregosa, P. van Mulbregt, SciPy 1. 0 Contributors, SciPy 1.0: fundamental algorithms for scientific computing in Python, Nature Methods 17 (2020) 261–272, aDS Bibcode: 2020NatMe..17..261V. doi:10.1038/s41592-019-0686-2.
URL https://ui.adsabs.harvard.edu/abs/2020NatMe..17..261V

[43] G. Buzsáki, Two-stage model of memory trace formation: a role for "noisy" brain states, Neuroscience 31 (3) (1989) 551–570. doi:10.1016/0306-4522(89)90423-5.

[44] M. L. V. Quyen, A. Bragin, R. Staba, B. Crépon, C. L. Wilson, J. Engel, Cell Type-Specific Firing during Ripple Oscillations in the Hippocampal Formation of Humans, Journal of Neuroscience 28 (24) (2008) 6104–6110, publisher: Society for Neuroscience Section: Brief Communications. doi:10.1523/JNEUROSCI.0437-08.2008.
URL https://www.jneurosci.org/content/28/24/6104

[45] N. Hájos, M. R. Karlócai, B. Németh, I. Ulbert, H. Monyer, G. Szabó, F. Erdélyi, T. F. Freund, A. I. Gulyás, Input-output features of anatomically identified CA3 neurons during hippocampal sharp wave/ripple oscillation in vitro, The Journal of Neuroscience: The Official Journal of the Society for Neuroscience 33 (28) (2013) 11677–11691. doi:10.1523/JNEUROSCI.5729-12.2013.

[46] E. W. Schomburg, C. A. Anastassiou, G. Buzsáki, C. Koch, The Spiking Component of Oscillatory Ex-

tracellular Potentials in the Rat Hippocampus, The Journal of Neuroscience 32 (34) (2012) 11798–11811. `doi:10.1523/JNEUROSCI.0656-12.2012`.
URL `https://www.ncbi.nlm.nih.gov/pmc/articles/PMC3459239/`

[47] G. Buzsáki, Hippocampal sharp wave-ripple: A cognitive biomarker for episodic memory and planning, Hippocampus 25 (10) (2015) 1073–1188, _eprint: https://onlinelibrary.wiley.com/doi/pdf/10.1002/hipo.22488. `doi:https://doi.org/10.1002/hipo.22488`.
URL `https://onlinelibrary.wiley.com/doi/abs/10.1002/hipo.22488`

[48] X. Liu, S. Ramirez, P. T. Pang, C. B. Puryear, A. Govindarajan, K. Deisseroth, S. Tonegawa, Optogenetic stimulation of a hippocampal engram activates fear memory recall, Nature 484 (7394) (2012) 381–385, number: 7394 Publisher: Nature Publishing Group. `doi:10.1038/nature11028`.
URL `https://www.nature.com/articles/nature11028`

[49] M. K. van Vugt, A. Schulze-Bonhage, B. Litt, A. Brandt, M. J. Kahana, Hippocampal Gamma Oscillations Increase with Memory Load, The Journal of Neuroscience 30 (7) (2010) 2694–2699. `doi:10.1523/JNEUROSCI.0567-09.2010`.
URL `https://www.ncbi.nlm.nih.gov/pmc/articles/PMC2835496/`

[50] K. Nader, Memory traces unbound, Trends in Neurosciences 26 (2) (2003) 65–72. `doi:10.1016/S0166-2236(02)00042-5`.
URL `https://www.sciencedirect.com/science/article/pii/S0166223602000425`

[51] K. Diba, G. Buzsáki, Forward and reverse hippocampal place-cell sequences during ripples, Nature Neuroscience 10 (10) (2007) 1241–1242, number: 10 Publisher: Nature Publishing Group. `doi:10.1038/nn1961`.
URL `https://www.nature.com/articles/nn1961`

Contributors

Y.W. and T.Y. conceptualized the study; Y.W. performed the data analysis; Y.W. and T.Y. wrote the original draft; and all authors reviewed the final manuscript.

Acknowledgments

Declaration of Interests

The authors declare that they have no competing interests.

Data and code availability

The data is available on G-Node (`https://doi.gin.g-node.org/10.12751/g-node.d76994/`).
The source code is available on GitHub (`https://github.com/yanagisawa-lab/hippocampal-neural-fluctuation-during-a-WM-task-in-hum`

Inclusion and Diversity Statement

We support inclusive, diverse, and equitable conduct of research.

Declaration of Generative AI in Scientific Writing

The authors employed ChatGPT, provided by OpenAI, for enhancing the manuscript's English language quality. After incorporating the suggested improvements, the authors meticulously revised the content. Ultimate responsibility for the final content of this publication rests entirely with the authors.

Tables

Subject ID	of sessions	AHL	AHR	PHL	PHR	ECL	ECR	AL	AR	SOZ
1	4	o	x	o	o	o	x	o	x	"AHR, LR"
2	7	o	o	o	o	o	o	o	o	"AHR, PHR"
3	3	o	o	o	o	o	o	o	x	"AHL, PHL"
4	2	o	o	o	o	o	o	o	o	"AHL, AHR, PHL, PHR"
5	3	o	x	x	o	x	x	o	x	DRR
6	6	o	o	o	o	o	o	o	o	"AHL, PHL, ECL, AL"
7	4	o	o	o	o	o	o	o	o	"AHR, PHR"
8	5	o	o	o	o	o	o	o	o	ECR
9	2	o	o	o	o	o	o	o	o	"ECR, AR"

Table 1 – Electrode Positions in the Dataset

Annotation of electrode positions and seizure onset zones: regions depicted with an "o" symbol are included, while those marked with an "x" (*navy*) are omitted from the dataset. Abbreviations: AHL denotes left hippocampal head; AHR represents right hippocampal head; PHL signifies left hippocampal body; PHR indicates right hippocampal body; ECL refers to left entorhinal cortex; ECR implies right entorhinal cortex; AL refers to left amygdala; AR stands for right amygdala; SOZ pertains to seizure onset zone [35].

Subject	AHL	AHR	PHL	PHR
1	0.60 ± 0.14	n.a.	n.a.	0.1 ± 0
2	0.21 ± 0.16	0.17 ± 0.21	0.18 ± 0.22	0.20 ± 0.15
3	0.40 ± 0.42	0.83 ± 0.12	n.a.	n.a.
4	0.10 ± 0.00	0.10 ± 0.00	0.90 ± 0.00	0.10 ± 0.14
5	n.a.	n.a.	n.a.	n.a.
6	0.63 ± 0.06	n.a.	n.a.	0.27 ± 0.06
7	0.10 ± 0.00	0.35 ± 0.35	0.37 ± 0.47	0.10 ± 0.00
8	0.13 ± 0.10	n.a.	0.28 ± 0.49	n.a.
9	n.a.	0.85 ± 0.07	0.15 ± 0.07	n.a.

**Table 2 – Silhouette score comparison of UMAP clustering between SWR^+ candidates and SWR^- candidates**

The silhouette scores (mean ± SD across sessions by subject) of UMAP clustering for SWR$^+$ candidates and SWR$^-$ candidates (Figure 4A) were derived from their underlying multiunit spike patterns. The mean values were recorded as 0.205 (SD = 0.285), with a median within an interquartile range (IQR; Figure 4B) [40, 41].

Subject ID	of sessions	of trials	ROI	of SWRs	SWR incidence [Hz]
1	2	100	AHL	274	0.34
3	2	97	AHR	325	0.42
4	2	99	PHL	202	0.26
6	2	100	AHL	297	0.37
9	2	97	AHR	72	0.09
Total = 10	Total = 493	"Total = 1,170"	0.30 ± 0.13 (mean ± SD)		

Table 3 – Count of Identified SWR Events

The table displays the summary statistics of the presumptive CA1 regions and SWRs. To mitigate sampling bias, solely the initial two sessions (sessions 1 and 2) from each subject were employed.
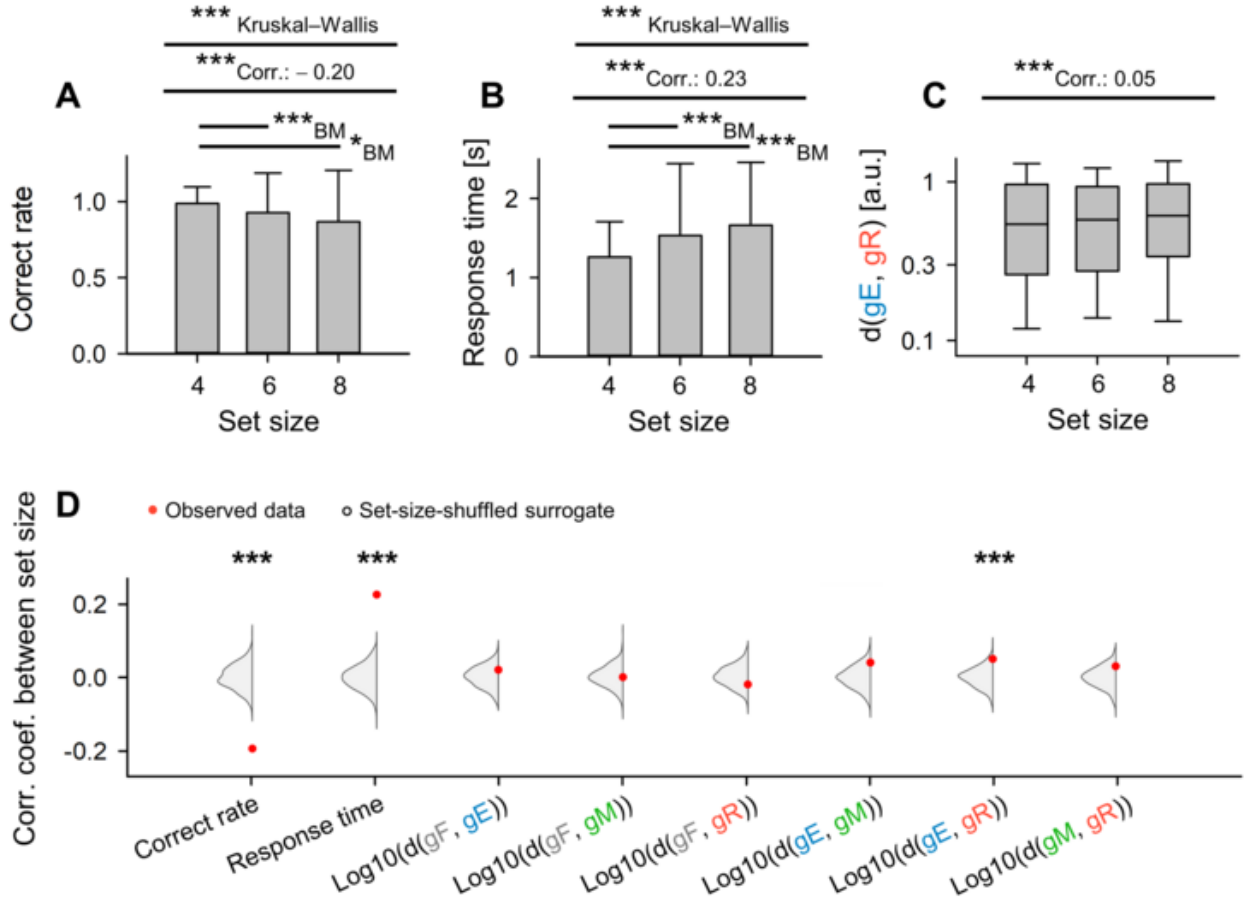
Figures
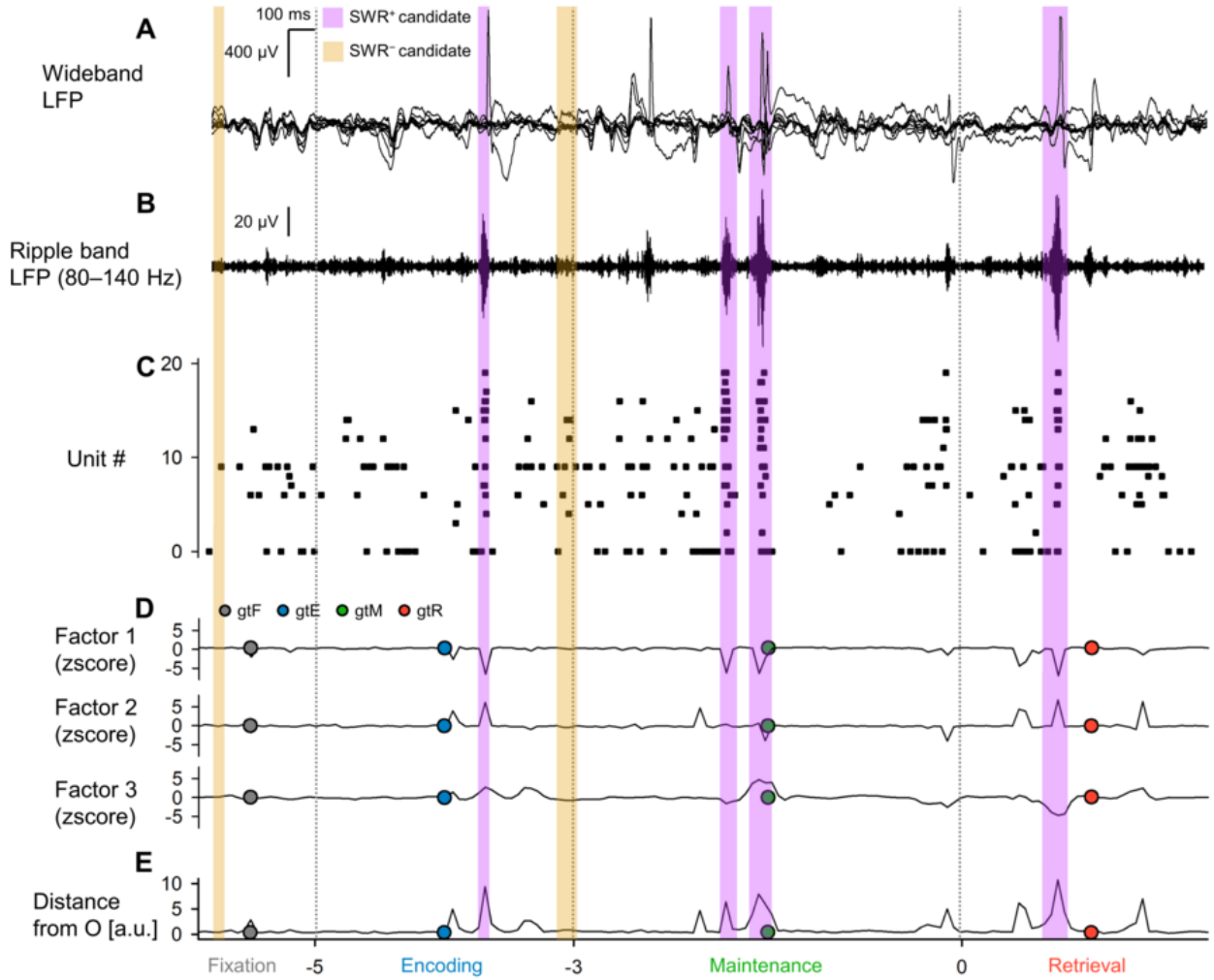
Figure 1 – Local field potential (LFP), multiunit activity, and neural trajectory of the hippocampus during a modified Sternberg task [8**?** , 9]

A. Representative wideband LFP traces from iEEG signals recorded in the left hippocampal head. These were attained while the subject performed a modified Sternberg working memory task, consisting of fixation (1 s, *gray*), encoding (2 s, *blue*), maintenance (3 s, *green*), and retrieval (2 s, *red*) [8**?** , 9]. *B.* The corresponding ripple band LFP traces [46, 21, 22]. *C.* The raster plot of multiunit spikes derived from the LFP traces using a spike sorting algorithm [37]. *D.* Neural trajectory determined by GPFA on the basis of spike counts per unit with 50-ms bins [36]. The dot circles represent the geometric median coordinates for each phase. *E.* Trajectory distance from the origin *O*. Please note that the *purple* and *yellow* rectangles indicate the timings for SWR$^+$ candidates and SWR$^-$ candidates (controls for SWR$^+$), respectively [49, 1, 39, 50, 10, 11, 12].

15

Figure 2 – State-dependent hippocampal neural trajectory

A. The neural trajectory in the first three-dimensional factors computed using GPFA is illustrated. Smaller dots represent the coordinates of 50-ms neural trajectory bins, while larger dots outlined in *black* denote the geometric medians for subsequent phases in the Sternberg working memory task: fixation (*gray*), encoding (*blue*), maintenance (*green*), and retrieval (*red*)[36]. *B.* This figure demonstrates the log-likelihood of GPFA models in conjunction with the number of dimensions employed to embed multi-unit spikes in MTL regions. Significantly, the optimal dimension was determined to be three, ascertained through the use of the elbow method[42]. *C.* In this segment, the distance of neural trajectory is mapped from the origin (*O*) for the hippocampus (Hipp.), entorhinal cortex (EC), and amygdala (Amy.), and is plotted in relation to the time from the probe's commencement[35]. *D.* The following graph illustrates the trajectory distance from *O* within MTL regions, whereby the hippocampus exhibits the greatest distance, succeeded by the EC and the Amygdala[16]. *E.* The subsequent representation indicates inter-phase trajectory distances within the MTL regions[38]. Abbreviations:

Figure 3 – Dependence of Trajectory Distance on Memory Load Between Encoding and Retrieval States in the Hippocampus

A. Set size (the number of letters to encode) and correct rate in the WM task (coefficient = −0.20, ***$p < 0.001$) [49, 8, 7]. *B.* Set size and response time (coefficient = 0.23, ***$p < 0.001$) [9]. *C.* Set size and the inter-phase distances between encoding and retrieval phases ($\|g_E g_R\|$) (correlation coefficient = 0.05) [8]. *D. Red* dots illustrate experimentally observed correlations between set size and the following parameters: correct rate, response time, $\log_{10} \|g_F g_E\|$, $\log_{10} \|g_F g_M\|$, $\log_{10} \|g_F g_R\|$, $\log_{10} \|g_E g_M\|$, $\log_{10} \|g_E g_R\|$, and $\log_{10} \|g_M g_R\|$. The *gray* kernel density plot indicates corresponding set-size-shuffled surrogate ($n = 1{,}000$) (***ps < 0.001) [22, 45].

Figure 4 – Detection of SWRs in Presumed CA1 Regions

A. Two-dimensional UMAP (uniform manifold approximation and projection) projection of multiunit spikes during candidates for SWRs (*purple*) and non-SWRs (*yellow*)[40]. *B.* Cumulative density plot of silhouette scores, utilized as a gauge for UMAP clustering quality, for hippocampal regions (refer to Table 2). Lands exceeding a silhouette score of 0.60 (equating to the 75th percentile) were classified as probable CA1 regions. Candidates for SWRs and non-SWRs identified in these hypothetical CA1 regions were defined as SWRs and non-SWRs (*n*s = 1,170), respectively[41]. *C.* The distribution of durations for both SWRs (*purple*) and non-SWRs (*yellow*) are congruent, given their definitions (93.0 [65.4] ms, median [IQR])[14][20]. *D.* SWR incidence for SWRs (*purple*) and non-SWRs (*yellow*) over time from probing, represented as a mean value ±95% confidence interval. Despite their singular character, the intervals may not be visible due to their narrowness. Note that a significant uptake in SWR incidence was perceived during the first 400 ms of the retrieval phase (0.421 [Hz], *p* < 0.05, bootstrap test)[47][15][16]. *E.* The distributions of ripple band peak amplitudes are presented for non-SWRs (*yellow*; 2.37 [0.33] SD of baseline, median [IQR]) and SWRs (*purple*; 3.05 [0.85] SD of baseline, median [IQR]) (***p < 0.001, utilizing the Brunner–Munzel test)[19][51][38].
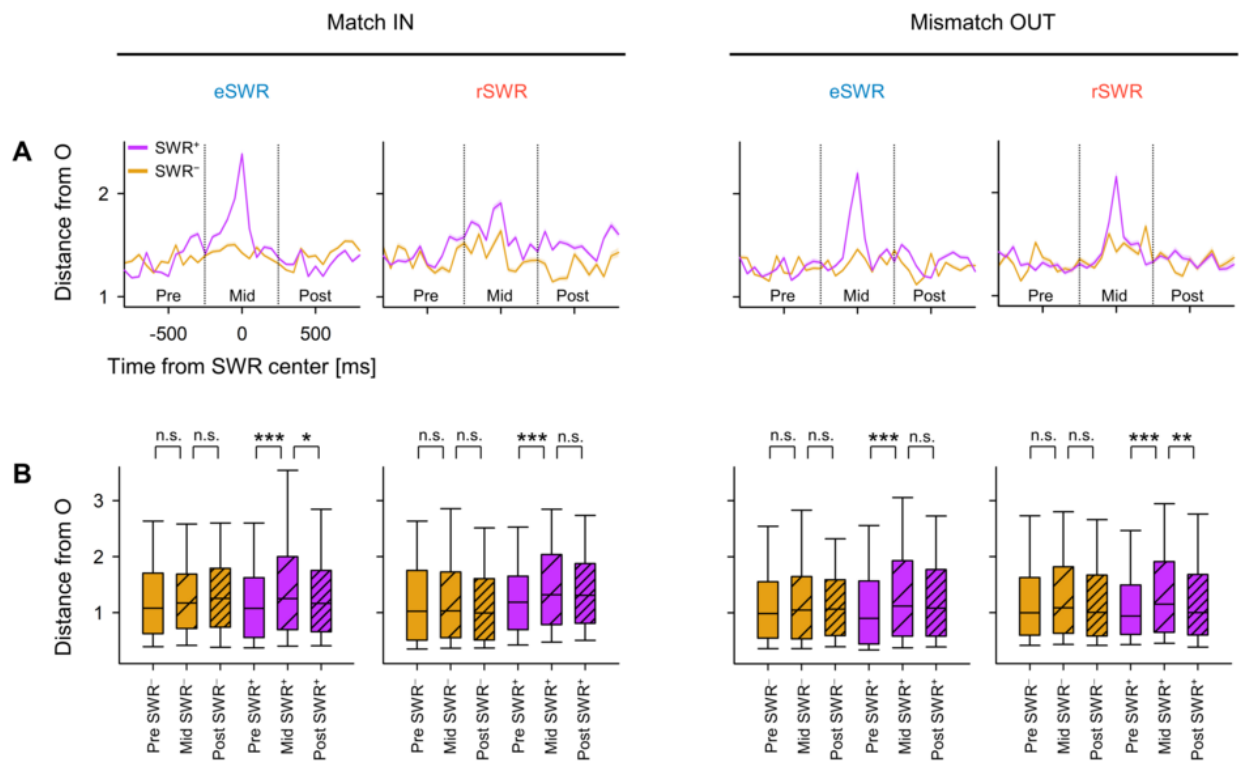
Figure 5 – Transient Alterations in Neural Trajectory During SWR

A. Represents the distance from the origin (*O*) of the peri-sharp-wave-ripple (SWR) trajectory expressed as the mean ±a 95% confidence interval, which may not be visible owing to its narrow range [14, 19, 47]. **B.** Illustrates the distance from the origin (*O*) during the pre-, mid-, and post-SWR periods (*$p < 0.05$, **$p < 0.01$, ***$p < 0.001$; according to the Brunner–Munzel test [3]). Abbreviations detailed as: SWR, sharp-wave ripple events; eSWR, SWR occurring in the encoding phase; rSWR, SWR happening during the retrieval phase; SWR$^+$, SWR event; SWR$^-$, control events for SWR$^+$; pre-, mid-, or post-SWR, the time intervals from -800 to -250 ms, from -250 to $+250$ ms, or from $+250$ to $+800$ ms, each relative to the SWR center.
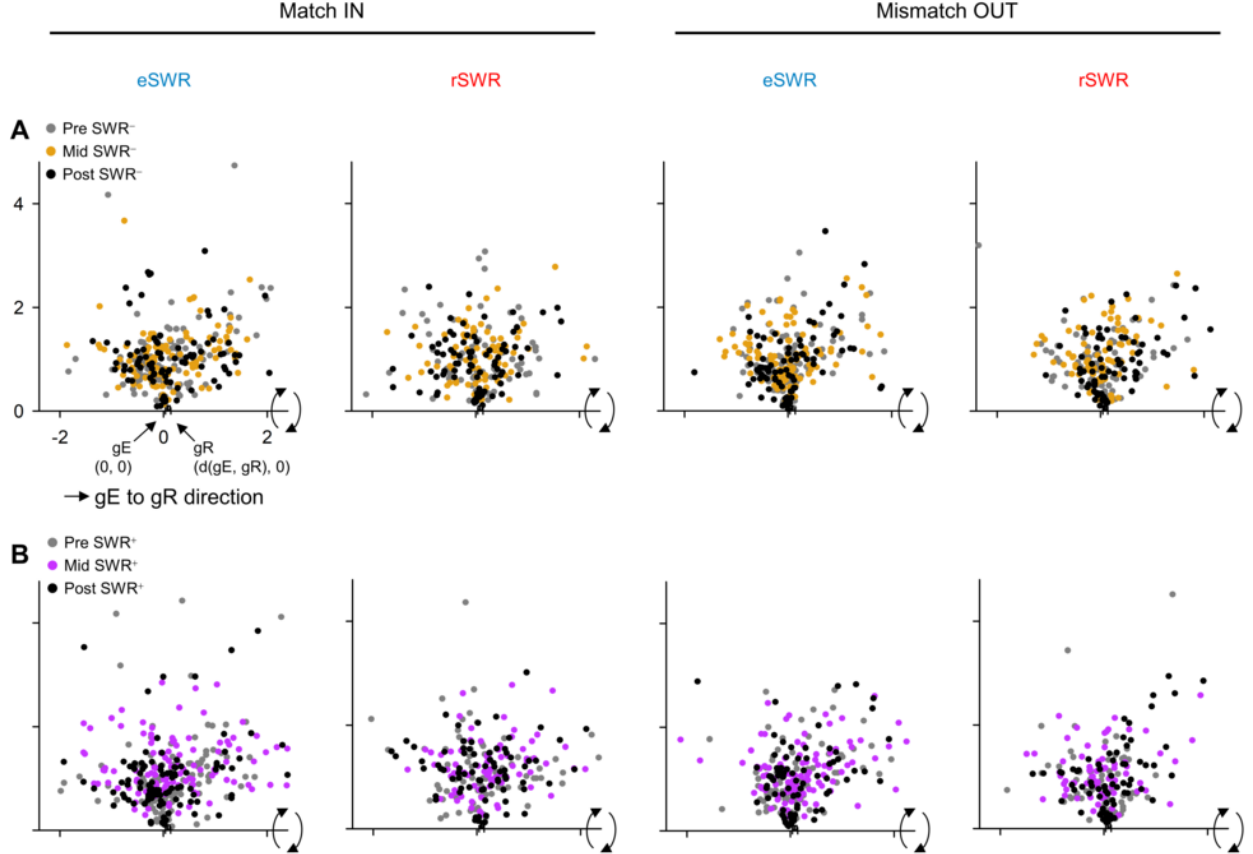
Figure 6 – Visualization of Neural Trajectory During SWR in Two-Dimensional Space

Featured are neural trajectories within the hippocampus during Sharp-Wave Ripple (SWR) events, represented in a two-dimensional space. **A.** Trajectories during pre- (*gray*), mid- (*yellow*), and post-SWR$^-$ (*black*) phases of an SWR event [47]. **B.** Corresponding trajectories for SWR$^+$ scenarios as opposed to SWR$^-$ [16]. The magnitude of $\|g_E g_R\|$ fluctuates within sessions [38]. The projection protocol went as follows: initially, g_E was placed at the origin O (0,0), and g_R at ($\|g_E g_R\|$, 0) via linear transformation [17]. Subsequently, the point cloud was rotated around the $g_E g_R$ axis (the x-axis) for compatibility with a two-dimensional environment [36]. Consequently, both the distances from O and the angles with respect to the $g_E g_R$ axis were kept intact from their original three-dimensional arrangement [40]. Abbreviations: SWR denotes Sharp-Wave Ripple events; eSWR refers to SWR during the encoding phase; rSWR indicates SWR during the retrieval phase; SWR$^+$ represents an SWR event; SWR$^-$ designates the control events for SWR$^+$; pre-SWR, mid-SWR, or post-SWR specify the time interval from -800 to -250 ms, from -250 to $+250$ ms, or from $+250$ to $+800$ ms from the center of the SWR respectively [30].

Figure 7 – Neural Trajectory Directions of SWR based on Encoding and Retrieval States

A–B Kernel Density Estimation (KDE) distribution of $\overrightarrow{\text{eSWR}^+} \cdot \overrightarrow{\text{rSWR}^+}$ (*pink circles*), $\overrightarrow{\text{eSWR}^+} \cdot \overrightarrow{\text{g}_E\text{g}_R}$ (*blue triangles*), and $\overrightarrow{\text{rSWR}^+} \cdot \overrightarrow{\text{g}_E\text{g}_R}$ (*red rectangles*) in Match IN (*A*) and Mismatch OUT tasks (*B*) [8]. *C–D* The corresponding distributions of SWR$^-$ replace those of SWR$^+$ in *A–B* [9]. *E–F* The differences in distributions of SWR$^+$ and SWR$^-$, emphasizing the SWR components (*E = C − A; F = B − D*). Notice the biphasic distributions of $\overrightarrow{\text{rSWR}^-} \cdot \overrightarrow{\text{g}_E\text{g}_R}$, underscoring neural fluctuations between encoding and retrieval states during the Sternberg task [7]. Conversely, in the Mismatch OUT task, inverse directionality between $\overrightarrow{\text{eSWR}^+}$ and $\overrightarrow{\text{rSWR}^+}$ (*pink circles*) was identified, but not in the Match IN task (*E–F*) [31, 32]. Lastly, transitions from retrieval to encoding states were observed for the SWR components in both Match IN and Mismatch OUT tasks (*red rectangles* in *E–F*) [37, 46].